block to further progress in the study of non–El Niño climate variability (*23*, *24*). Our results demonstrate that surface winds react to modest subtropical SST variations as small as a few tenths of a degree. The simulation of the far-reaching effects of Hawaii can serve as a test for the next generation of high-resolution climate models.

The physical processes we have described here probably give rise to other changes in the Pacific Ocean and atmosphere. For instance, Hawaii, with its volcanic and human activities, is a major aerosol source for the surrounding region. The long convergence line in the wind wake detected in this study may influence the transport of aerosols and trace gases in the PBL and their exchange with the free atmosphere. Regarding the ocean, the banded structures in upwelling velocity may lead to variations in the distributions of plankton and other fishery resources.

References and Notes

1. R. B. Smith, A. C. Gleason, P. A. Gluhosky, V. Grubisic, *J. Atmos. Sci.* **54**, 606 (1997).
2. M. H. Freilich, Orographically Modified Winds Observed by the NASA Scatterometer (1997) (available at www.oce.orst.edu/po/research/mhf/).
3. K. P. Chopra, *Adv. Geophys.* **16**, 298 (1973).
4. D. Etling, *Meteorol. Atmos. Phys.* **41**, 157 (1989).
5. T. P. DeFelice, D. J. Meyer, G. Xian, J. Christopherson, R. Cahalan, *Bull. Am. Meteorol. Soc.* **81**, 1047 (2000).
6. W. T. Liu, X. Xie, P. S. Polito, S.-P. Xie, H. Hashizume, *Geophys. Res. Lett.* **27**, 2545 (2000).
7. The winds on and near the Big Island have been the focus of previous field campaigns (*25*, *26*). Reduced wind speed on the windward side of the Big Island results from orographic blocking (Fig. 1). The strongest winds are found between Maui and the Big Island, reaching 11 m/s in the monthly-mean map of Fig. 1 in comparison to the ambient speed of 7 m/s. The winds between these two tallest islands can often exceed 20 m/s, and these strong winds are blamed for having damaged the foremast of the ship *Resolution* in 1779, forcing Captain James Cook to make his fatal return trip to the Big Island. The strong positive wind curl probably contributes to the formation of the cold eddies often observed northwest of the Big Island (*27*).
8. Supplementary Web material is available on *Science* Online at www.sciencemag.org/cgi/content/full/292/5524/2057/DC1.
9. F. J. Wentz, C. Gentemann, D. Smith, D. Chelton, *Science* **288**, 847 (2000).
10. S.-P. Xie, S. G. H. Philander, *Tellus* **46A**, 340 (1994).
11. P. Chang, L. Ji, H. Li, *Nature* **385**, 516 (1997).
12. T. Yamagata, in *Coupled Ocean-Atmosphere Model*, J. C. J. Nihoul, Ed. (Elsevier, New York, 1985), pp. 637–657.
13. B. Qiu, D. A. Koh, C. Lumpkin, P. Flament, *J. Phys. Oceanogr.* **27**, 431 (1997).
14. P. Flament, S. Kennan, R. Lumpkin, M. Sawyer, E. Stroup, in *Atlas of Hawaii*, S. P. Juvik, J. O. Juvik, Eds. (Univ. of Hawaii Press, Honolulu, HI, 1998), pp. 82–86.
15. D. Stammer, R. Tokmakian, A. J. Semtner, C. Wunsch, *J. Geophys. Res.* **101**, 25779 (1996).
16. Q. Liu, H. Yang, H. Bao, W. Li, *Chin. J. Atmos. Sci.* **24**, 363 (2000).
17. S.-P. Xie, T. Kunitani, A. Kubokawa, M. Nonaka, S. Hosoda, *J. Phys. Oceanogr.* **30**, 2798 (2000).
18. K. Yoshida, T. Kidokoro, *J. Oceanogr. Soc. Jpn.* **23**, 88 (1967).
19. K. Takeuchi, *J. Phys. Oceanogr.* **16**, 919 (1986).
20. A. Kubokawa, T. Inui, *J. Phys. Oceanogr.* **29**, 1303 (1999).
21. West of Hawaii, ocean current direction is especially sensitive to the curl of the wind wake off the islands, because the large-scale Ekman pumping field has little meridional gradient (Fig. 4B) to drive background zonal current.
22. The existing in situ measurements are insufficient to ascertain the western extent of the eastward countercurrent that ends at Hawaii, but a hydrographic section maintained by the Japan Meterological Agency along 137°E since 1967 hints at its existence in the far western Pacific. Geostrophic calculation using the long-term mean data in this 137°E section indicates that at 19°N, the eastward shear reaches a meridional maximum in the upper 300 m, and the current, albeit weak, is eastward near the surface (*28*). The use of new satellite data here allows us to determine for the first time that the high mountains on the Hawaiian Islands, by blocking the air flow, are the ultimate cause of this eastward countercurrent along 19°N [appendix C in (*8*)].
23. Y. Okumura, S.-P. Xie, A. Numaguti, Y. Tanimoto, *Geophys. Res. Lett.* **28**, 1507 (2001).
24. W. A. Robinson, *Bull. Am. Meteorol. Soc.* **77**, 567 (2000).
25. R. B. Smith, V. Grubisic, *J. Atmos. Sci.* **50**, 3728 (1993).
26. E. C. Nickerson, M. A. Dias, *J. Appl. Meteorol.* **20**, 868 (1981).
27. W. C. Patzert, *Hawaii Inst. Geophys. Rep. 69-8* (1969).
28. W. B. White, A. E. Walker, *J. Geophys. Res.* **90**, 7061 (1985)
29. E. Kalnay *et al.*, *Bull. Am. Meteorol. Soc.* **77**, 437 (1996).
30. W. B. White, *Progr. Oceanogr.* **36**, 169 (1995).

31. We thank B. Qiu and G. Speidel for comments and W. Tang, X. Xie, A. Pan, P. Broccio, R. Tokmakian, H. Okajima, Y. Okumura and J. Hafner for data processing and graphics. The Special Sensor Microwave/Imager and TRMM data were produced by F. Wentz at Remote Sensing Systems, who generously made them openly accessible. The European Remote-Sensing Satellite data were obtained via FTP from the Institut Français de Recherche pour l'Exploitation de la Mer. This study is supported by NASA under QuikSCAT and TRMM missions and grant NAG5-10045, by the Frontier Research System for Global Change, and by the National Natural Science Foundation of China (grant 49976004). W.T.L.'s work was performed at the Jet Propulsion Laboratory, California Institute of Technology, under contract with NASA. This is International Pacific Research Center contribution 92 and School of Ocean and Earth Science and Technology contribution 5579.

12 February 2001; accepted 7 May 2001

Linearly Polarized Emission from Colloidal Semiconductor Quantum Rods

Jiangtao Hu,[1,2]* Liang-shi Li,[1,2]* Weidong Yang,[1,2] Liberato Manna,[1,2] Lin-wang Wang,[3] A. Paul Alivisatos[1,2]†

Colloidal quantum rods of cadmium selenide (CdSe) exhibit linearly polarized emission. Empirical pseudopotential calculations predict that slightly elongated CdSe nanocrystals have polarized emission along the long axis, unlike spherical dots, which emit plane-polarized light. Single-molecule luminescence spectroscopy measurements on CdSe quantum rods with an aspect ratio between 1 and 30 confirm a sharp transition from nonpolarized to purely linearly polarized emission at an aspect ratio of 2. Linearly polarized luminescent chromophores are highly desirable in a variety of applications.

Colloidal semiconductor nanocrystals, or quantum dots, are a class of luminescent chromophores, which has emerged from the growing fields of nanoscience and nanotechnology (*1*, *2*). The optical emission properties of these chromophores can be tailored by suitably adjusting the height, width, and shape of the potential that confines electrons and holes. In spherically shaped colloidal dots, the band gap and oscillator strength can be tuned by variation of the diameter (*3*). Colloidal dots can be produced by comparatively simple solution methods and are photochemically robust (*4*, *5*). Compared to self-assembled quantum dots made by molecular beam epitaxy (*6*, *7*), they have more chemical flexibility and have nearly the same optical and electrical performance (*8*, *9*). Thus, colloidal quantum dots may have a very wide range of applications, e.g., as light emitters in biological labeling (*10*, *11*), displays (*12*, *13*), and lasers (*14*).

A limiting feature of the spherical colloidal dots is that their emission is not linearly polarized (*15*, *16*). It has been suggested that colloidal rods may display polarized emission with significant advantages over spherical dots (*17*). Here, we combine recent advances in synthetic control of nanocrystal shapes, single-molecule spectroscopy, and electronic structure theory to study quantum rods. We studied CdSe nanocrystals because their synthesis has been well developed (*18*, *19*), so much so that they have become a model system for studying quantum size effects. Theory predicts a level crossing as a function of aspect ratio in colloidal quantum rods, such that slightly elongated dots (an aspect ratio of 2:1) should emit linearly polarized light. This prediction is qualitatively verified by

[1]Department of Chemistry, University of California at Berkeley, Berkeley, CA 94720, USA. [2]Materials Science Division, [3]National Energy Research Scientific Computing Center, Lawrence Berkeley National Laboratory, 1 Cyclotron Road, Berkeley, CA 94720, USA.

*These authors contributed equally to this work.
†To whom correspondence should be addressed.

polarization experiments on light emission from single colloidal CdSe quantum rods. Thus, even a very modest change in the dots renders them far more useful in a wide range of optical emitter applications. Because the dots need only to be slightly elongated, the chemical flexibility is not compromised, as might be the case for very long rods. The success of the theory in predicting the crossover also suggests that it will be possible to predict the optical properties of the more complex shapes of nanocrystals that can now be produced, such as arrows and tetrapods (*20*).

The electronic structure of CdSe quantum dots has been studied theoretically with effective mass approximation models (*15, 21, 22*) and, more recently, with empirical pseudopotential methods (*23*). Qualitatively, the lowest excited electronic state of the bulk CdSe semiconductor arises when an electron is excited from an occupied Se 4p atomic orbital to an empty Cd 5s orbital. This excitation is distributed throughout many unit cells of the solid, and there is a pronounced dependence of the band gap on the size of the crystals. Because the p atomic orbitals are degenerate, the interaction between Se 4p orbitals in the crystal field and the effect of spin-orbit coupling contribute to most of the complexity in the electronic structure of CdSe nanocrystals.

An empirical pseudopotential calculation (*23*) was performed to study the evolution of the electronic structure when CdSe nanocrystals evolve from a spherical to a rodlike shape. We started from a spherical dot with a diameter of 3.0 nm and increased the aspect ratio by inserting a cylindrical segment along the *c* axis. The pseudopotentials of the Cd and Se atoms were obtained by fitting the band structure of bulk CdSe, and "ligand potentials" were added to surface atoms to remove the surface levels from the band gap (*23*). The four lowest unoccupied and four highest occupied electronic states were calculated for quantum rods with aspect ratio ranging from 1:1 to 5:1. As the aspect ratio increases from unity, a crossover of the two highest occupied electronic states occurs at an aspect ratio of 1.25 (Fig. 1). Before this point, the electronic states with predominantly Se $4p_x$, $4p_y$ components have higher energy than that of states that are mainly $4p_z$. The electronic energy levels of these states all increase with increasing size. The $4p_z$ orbital has greater momentum projected onto the *c* axis of the crystal compared to $4p_x$ and $4p_y$, so the energy levels with a greater $4p_z$ component are more sensitive to the rod length. These states exchange position relative to each other at an aspect ratio greater than 1.25. Calculations for the cases of 2.1- and 3.8-nm-wide rods show similar results, and the crossing points are 1.25 and 1.36, respectively.

This model thus predicts a sharp transition from plane-polarized emission to highly linearly polarized emission when the nanocrystals change from spherical to rodlike, even for an aspect ratio of not much greater than unity. Furthermore, this model also suggests that the global Stokes shift [the energy difference between the first ultraviolet-visible (UV-Vis) absorption peak and the luminescence peak of the nanocrystals] should at first decrease and then increase as a function of the aspect ratio (Fig. 2A and text below). These two predictions of the empirical pseudopotential calculations are also qualitatively reproduced in eight-band effective-mass-approximation calculations (*24*).

In order to test these theoretical predictions, samples of quantum rods with very tightly controlled diameter and length are needed. Here, we report an improved procedure that yields a very narrow distribution of the rod diameter and length. Generally, CdSe quantum rods are made by pyrolysis of dimethylcadmium ($Cd(CH_3)_2$) and Se/tributyl phosphine (TBP) solution in hot trioctylphosphine oxide (TOPO) with the presence of hexylphosphonic acid (HPA) under inert gases (*17, 20*). On the basis of a recent observation (*25*) that the growth of CdSe quantum rods along the *c* axis is much slower when

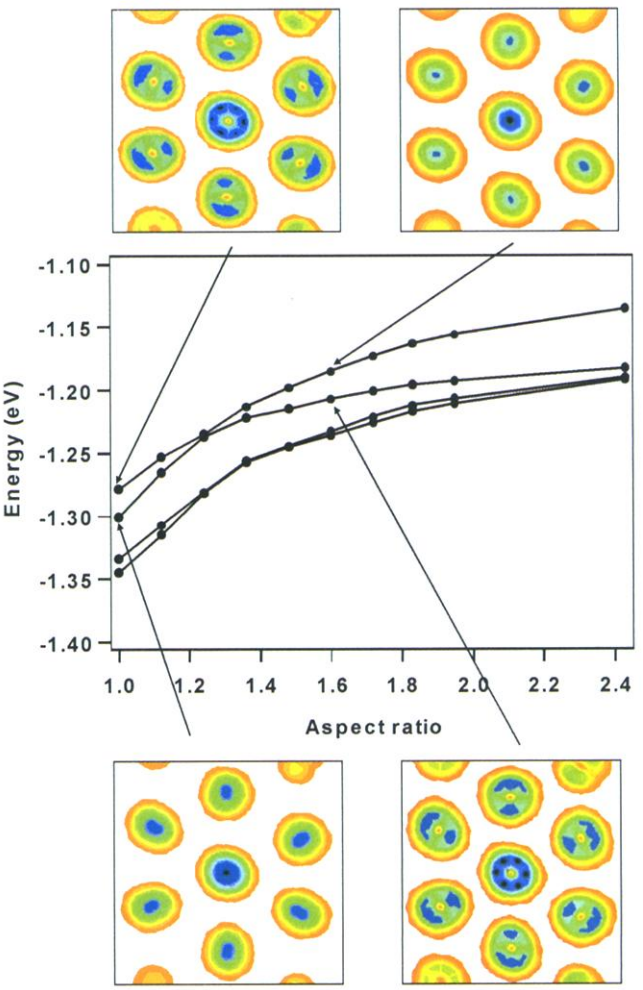

Fig. 1. The four highest occupied electronic states of 3.0-nm-diameter CdSe quantum rods calculated with an empirical pseudopotential method with different aspect ratios. The two highest energy levels have a crossing at an aspect ratio of ~1.25. The color images show the contour plots of the two highest occupied states for rods with aspect ratios of 1.00 and 1.60. They show the projection of electron density around some Se atoms in a plane, with density increasing from red to blue. This plane intersects the rod in the middle, perpendicular to the long axis (*c* axis). The crossing-over of the predominantly $p_{x,y}$ and predominantly p_z levels versus the aspect ratio can be seen.

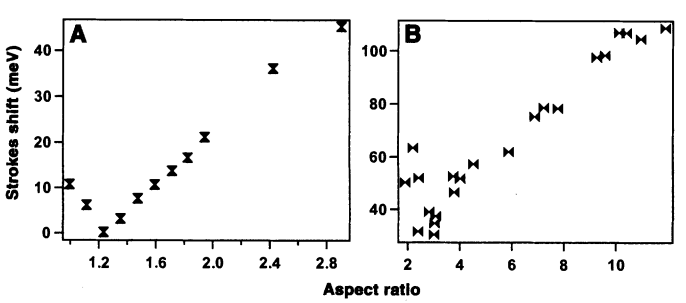

Fig. 2. Global Stokes shift versus aspect ratio. (**A**) Results from the calculated electronic energy levels for 3.0-nm-wide quantum rods. The absorption spectra are calculated as the sum of all possible transitions from the highest four occupied states to the lowest four unoccupied states (not shown) weighed by oscillator strengths (*33*), allowing a Gaussian distribution of lengths with a 10% standard deviation. The first maximum from the red edge is considered to be the first absorption peak. (**B**) Experimental results for quantum rods with diameters of 3.9 ± 0.2 nm. Rods with different widths show similar trends.

a phosphonic acid with a longer hydrocarbon chain [such as tetradecylphosphonic acid (TDPA)] is used, we used a mixture of these two phosphonic acids to adjust the growth rate along the *c* axis. In a typical synthesis, a mixture of HPA, TDPA, and TOPO was heated to 360°C under argon, $Cd(CH_3)_2$/TBP solution was added to the mixture dropwise, and then a quick injection of Se/TBP solution was made to initiate the crystal growth. Separate addition of Cd and Se precursors was critical for obtaining a narrow size distribution (*25*). After the injection, the solution was kept at 300°C for growth, and aliquots were taken out for optical measurements. The HPA/TDPA molar ratio, ranging from 3:1 to 1:3, very sensitively determines the diameter and aspect ratio of the rods at the beginning of the growth and the speed of shape evolution.

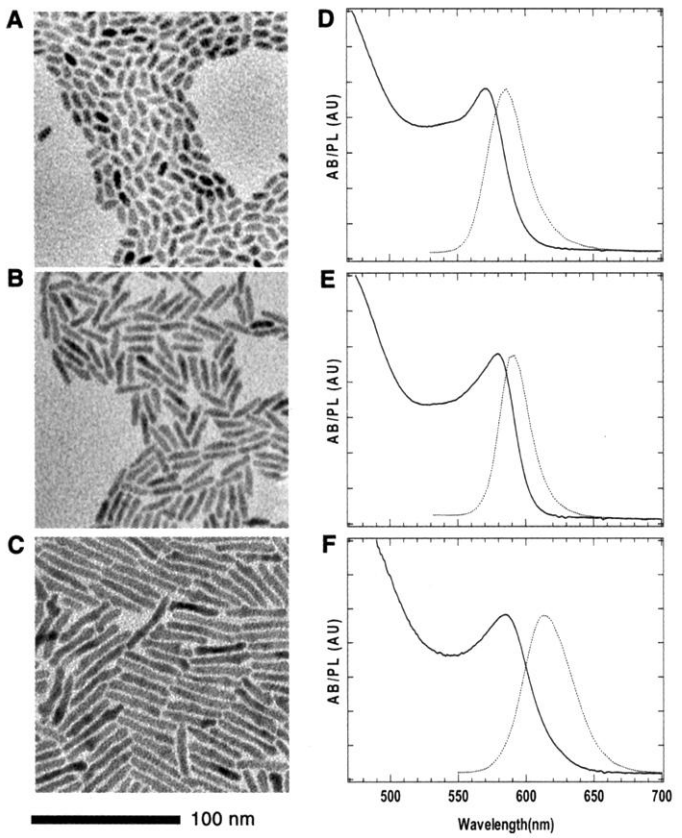

Fig. 3. (**A** through **C**) TEM images and (**D** through **F**) UV-Vis absorption (solid lines) and photoluminescence (dotted lines) spectra of three rod samples. Quantum rods with diameters of ~4.2 nm and lengths of 11 [(A) and (D)], 20 [(B) and (E)], and 40 nm [(C) and (F)].

Transmission electron microscopy (TEM) images of several typical CdSe rod samples are shown in Fig. 3, along with their absorption and emission spectra. The samples were taken from the solution during growth and washed to remove excess surfactant, but no size selective procedure was performed. The size distribution, as determined by measuring TEM images of more than 200 particles for each sample, was ~5% in diameter and <10% in length. The narrow size distribution is crucial for systematic studies of size and shape dependence of electronic and optical properties for both ensemble and single-particle measurements. The UV-Vis absorption and photoluminescence spectra on ensemble samples have peak widths comparable to those of spherical quantum dots (Fig. 3, D through F).

Single-dot luminescence spectroscopy was used to determine the polarization of their emission. We used a confocal fluorescence microscope similar to the one described in (*26*). A dilute solution of the nanoparticles in chloroform was spin cast onto a quartz substrate, and atomic force microscopy was used to make sure that individual rods are separated by at least 0.5 μm. We used a circularly polarized Ar^+ ion laser to excite the nanocrystals and a beam-displacing crystal to split the luminescence light into two perpendicularly polarized beams. The two split images are 2 cm apart and can be simultaneously recorded with a single charge-coupled device camera. By rotating the beam-displacing crystal, polarizations along any pair of angles can be determined (*27*). Images of luminescence from a single quantum rod with a 10:1 aspect ratio (Fig. 4A) demonstrate the change with detection angle of the relative intensity along the two perpendicular polarization directions. The polarization factor ρ for this rod sample is determined to be 86% by fitting the intensity ratio $r = (I_{//} - I_{\perp})/(I_{//} + I_{\perp})$ versus detection angle with a sinusoidal function (solid circles in Fig. 4B) ($I_{//}$, intensity parallel to the optical axis of beam-displacing crystal; $I_{\perp}$, intensity perpendicular to the optical axis). In comparison, the polarization factor of spherical dots is usually <10% (solid triangles in Fig. 4B). We measured samples with an aspect ratio from 1:1 to 30:1 at room temperature. The polarization factor changes rapidly from nearly zero to ~70% (e.g., $I_{//}$:$I_{\perp} \cong 5.5:1$) when the aspect ratio increases from 1:1 to 2:1, then remains almost constant afterward (Fig. 4C). At low temperature, polarization factors of emission from spherical quantum dots take random values between 0 and 1 because of the "dark" *c* axis and the random orientation of the dots on

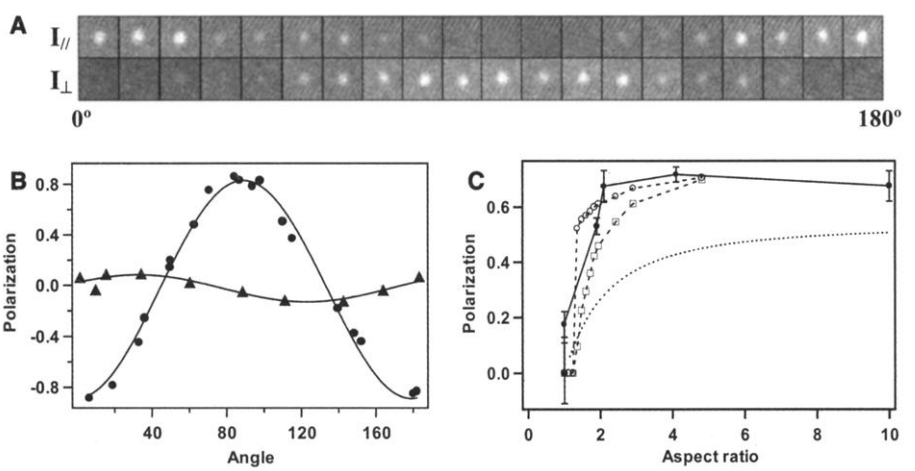

Fig. 4. Luminescence polarization measurements from individual quantum rods at room temperature. (**A**) Luminescence images of a single rod simultaneously recorded in two perpendicular polarization directions at detection angles changing from 0° to 180°. The rods have an aspect ratio of 10:1. (**B**) The intensity ratio $r = (I_{//} - I_{\perp})/(I_{//} + I_{\perp})$ calculated from the luminescence images in (A) (solid circles) and fitted with sinusoidal function (solid line) to give a polarization factor of 0.86. The data from spherical dots (solid triangles) show much smaller polarization factors. (**C**) Polarization factor versus aspect ratio. Solid circles with error bars (from statistics) are from experiments, open circles are from empirical pseudopotential calculations for 0 K, and squares are from empirical pseudopotential calculations for room temperature. Each experimental data point was obtained by measuring more than 40 individual rods. The lines simply connect data points, and the dotted line is from the fitting based on the dielectric model proposed in (*28*).

the substrate (*16*). However, the statistics for more than 40 spherical quantum dots in our measurement at room temperature shows that the average polarization factor is <10%. Because we used an objective lens with a large numerical aperture (e.g., 1.4) that depolarizes light, the limit for polarization factor that our experimental setup can obtain is ~80%. Thus, the emission from quantum rods with an aspect ratio greater than 2:1 is essentially purely linearly polarized, which is consistent with theoretical results.

To further test the calculations, we measured the global Stokes shift of the quantum rods experimentally. For rods with a fixed width, we found that the global Stokes shift decreased slightly from spherical dots to short rods and then increased with length to more than 100 meV, which is much greater than that of spherical quantum dots with the same diameter (Fig. 2B). This response qualitatively agrees with the theoretical results. A dielectric model was previously proposed to explain the anisotropic polarization of the emission from porous silicon, assuming that porous silicon is an aggregate of Si nanocrystals with different shapes (*28*). Concentration of the field lines in the region of high dielectric constant may contribute to the polarization of the emission from CdSe quantum rods as well (Fig. 4C). However, the nonmonotonic behavior of the Stokes shift versus the aspect ratio shows that the level crossing is the dominant factor at a small aspect ratio. A larger Stokes shift means a smaller overlap area between absorption and emission spectra, which is desirable in applications such as light-emitting diodes, where reabsorption reduces the total efficiency. We also see some discrepancies between the theory and experiments, however. The turning point from the experiments does not coincide with that from the theoretical calculations, and the experimental Stokes shift values are always greater than the theoretical ones. This difference could be due to factors such as the electric field caused by the dipole moment (*29, 30*) and the electron-phonon coupling (*31, 32*), which are not considered in the calculations.

The emission polarization of CdSe nanocrystals can be greatly modified by slightly changing their shapes without much of an increase in the complication of the preparation. This change greatly improves their potential in applications. The compression of emission to a single polarization axis makes these nanocrystals ideal for many orientation-sensitive applications. As emitters in lasers, CdSe quantum rods should increase power efficiency and lower the pumping threshold. They can also be used as labels in biological systems to study conformational change and energy transfer. Furthermore, the anisotropic geometry of longer quantum rods makes it possible to align them on a flat surface over a large area and therefore makes it feasible to use them in polarized light–emitting diodes and flat panel displays.

References and Notes

1. A. P. Alivisatos, *Science* **271**, 933 (1996).
2. L. E. Brus, *Appl. Phys. A* **53**, 465 (1991).
3. A. P. Alivisatos, *J. Phys. Chem.* **100**, 13226 (1996).
4. M. A. Hines, P. Guyot-Sionnest, *J. Phys. Chem.* **100**, 468 (1996).
5. X. G. Peng *et al.*, *J. Am. Chem. Soc.* **119**, 7019 (1997).
6. R. Leon, P. M. Petroff, D. Leonard, S. Fafard, *Science* **267**, 1966 (1995).
7. J. Heydenreich *et al.*, *Phys. Rev. Lett.* **74**, 4043 (1995).
8. M. Danek *et al.*, *J. Cryst. Growth* **145**, 714 (1994).
9. C. B. Murray, C. R. Kagan, M. G. Bawendi, *Science* **270**, 1335 (1995).
10. M. Bruchez Jr., M. Moronne, P. Gin, S. Weiss, A. P. Alivisatos, *Science* **281**, 2013 (1998).
11. W. C. W. Chan, S. Nie, *Science* **281**, 2016 (1998).
12. V. Colvin, M. Schlamp, A. P. Alivisatos, *Nature* **370**, 354 (1994).
13. B. O. Dabbousi, M. G. Bawendi, O. Onotsuka, M. F. Rubner, *Appl. Phys. Lett.* **66**, 1316 (1995).
14. V. I. Klimov *et al.*, *Science* **290**, 314 (2000).
15. Al. Efros, *Phys. Rev. B* **46**, 7448 (1992).
16. S. A. Empedocles, R. Neuhauser, M. G. Bawendi, *Nature* **399**, 126 (1999).
17. X. Peng *et al.*, *Nature* **404**, 59 (2000).
18. C. B. Murray, D. J. Norris, M. G. Bawendi, *J. Am. Chem. Soc.* **115**, 8706 (1993).
19. X. G. Peng, J. Wickham, A. P. Alivisatos, *J. Am. Chem. Soc.* **120**, 5343 (1998).
20. L. Manna, E. C. Scher, A. P. Alivisatos, *J. Am. Chem. Soc.* **122**, 12700 (2000).
21. Al. Efros *et al.*, *Phys. Rev. B* **54**, 4843 (1996).
22. Al. Efros, M. Rosen, *Annu. Rev. Mater. Sci.* **30**, 475 (2000).
23. L.-W. Wang, A. Zunger, *Phys. Rev. B* **53**, 9579 (1996).
24. W. Yang *et al.*, unpublished results.
25. Z. A. Peng, X. G. Peng, *J. Am. Chem. Soc.* **123**, 1389 (2001).
26. T. Ha, T. A. Laurence, D. S. Chemla, S. Weiss, *J. Phys. Chem. B* **103**, 6839 (1999).
27. This scheme overcomes the intensity fluctuation of the luminescence from a single nanocrystal due to "blinking" and bleaching [M. Mirmal *et al.*, *Nature* **383**, 802 (1996)] and therefore can be used in room temperature measurements.
28. D. Kovalev *et al.*, *Appl. Phys. Lett.* **67**, 1585 (1995).
29. E. Rabani *et al.*, *J. Chem. Phys.* **110**, 5355 (1999).
30. M. Shim, P. Guyot-Sionnest, *J. Chem. Phys.* **111**, 6955 (1999).
31. M. C. Klein, F. Hache, D. Ricard, C. Flytzanis, *Phys. Rev. B* **42**, 11123 (1990).
32. A. P. Alivisatos *et al.*, *J. Chem. Phys.* **90**, 3463 (1989).
33. Supplemental Web material is available on *Science* Online at www.sciencemag.org/cgi/content/full/1060810/DC1.

34. We thank X. Peng for inspiring discussion and R. Zalpuri and G. Vrdoljak at the Electron Microscope Lab at the University of California, Berkeley, for assistance in TEM measurement. This work is supported by the Director, Office of Energy Research, Office of Science, and Division of Materials Sciences of the U.S. Department of Energy (DOE) under contract DE-AC03-76SF00098, by the NIH National Center for Research Resources (grant 1 R01 RR-14891-01) under the same DOE contract number, and by the Department of Defense Advanced Research Projects Agency under grant ONR N00014-99-1-0728. L.W. is supported by the Director, Office of Science, Division of Mathematical, Information, and Computational Science of DOE under contract DE-AC03-76SF00098. This research used resources of the National Energy Research Scientific Computing Center, which is supported by the Office of Science of DOE.

19 March 2001; accepted 18 April 2001
Published online 3 May 2001;
10.1126/science.1060810
Include this information when citing this paper.

Chiral Sign Induction by Vortices During the Formation of Mesophases in Stirred Solutions

Josep M. Ribó,[1]* Joaquim Crusats,[1] Francesc Sagués,[2] Josep Claret,[2] Raimon Rubires[1]

Achiral diprotonated porphyrins, forming homoassociates in aqueous solution, lead to spontaneous chiral symmetry breaking. The unexpected result is that the chirality sign of these homoassociates can be selected by vortex motion during the aggregation process. This result is confirmed by means of circular dichroism spectra. These experimental findings are rationalized in terms of the asymmetric influence of macroscopic forces on bifurcation scenarios and by considering the specific binding characteristics of the porphyrin units to form the homoassociates.

When thinking about chirality induction in physicochemical processes, one has to distinguish between two completely different scenarios. In the first one, typical of an organic chemistry context and commonly described according to the standard reaction coordinate picture, asymmetric induction arises from a polarization effect acting on the reaction path (*1*). The second situation corresponds to a spontaneous symmetry breaking scenario, according to which an excess of one of the enantiomers is always obtained, although with an unpredictable sign. By invoking generic principles of nonequilibrium phenomena, this last behavior is readily interpreted with the notion of bifurcation of an unstable

[1]Department of Organic Chemistry, [2]Department of Physical Chemistry, University of Barcelona, Martí i Franquès 1, 08028-Barcelona, Catalonia, Spain.

*To whom correspondence should be addressed. E-mail: jmr@qo.ub.es